Optics Communications 588 (2025) 131945

Contents lists available at ScienceDirect

Optics Communications

journal homepage: www.elsevier.com/locate/optcom

Imaging the photophysics of organic semiconductors using polarisation-resolved and near-field optical spectroscopies

James Kerfoot [a,**], Tyler James [b], Takashi Taniguchi [c], Kenji Watanabe [d], Peter H. Beton [b], Graham A. Rance [a,e,*], Michael W. George [e,***]

[a] Nanoscale and Microscale Research Centre (nmRC), University of Nottingham, University Park, Nottingham, NG7 2RD, UK
[b] School of Physics and Astronomy, University of Nottingham, University Park, Nottingham, NG7 2RD, UK
[c] Research Center for Electronic and Optical Materials, National Institute for Materials Science, 1-1 Namiki, Tsukuba, 305-0044, Japan
[d] Research Center for Materials Nanoarchitectonics, National Institute for Materials Science, 1-1 Namiki, Tsukuba, 305-0044, Japan
[e] School of Chemistry, University of Nottingham, University Park, Nottingham, NG7 2RD, UK

A B S T R A C T

Imaging techniques that enable the structure of organic semiconductors to be determined across length scales are essential for optimisation of their luminescence properties. In this study, we prepare well-ordered monolayer films of perylene-3,4,9,10-tetracarboxylic-3,4,9,10-diimide (PTCDI) both on the surface of hexagonal boron nitride (hBN) and confined within few-layer thick hBN vertical heterostructures, and apply polarisation-resolved and tip-enhanced optical spectroscopies to image the effects of molecular orientation and dielectric environment on the photoluminescence (PL) exhibited by this prototype organic semiconductor translated at the micro and nano length scales, respectively. Using this combined approach, we show that PTCDI self-assembles into two discrete types of few-micron-sized grains at sub-monolayer coverage, each exhibiting characteristic shifts in PL emission energy related to their registry on hBN surfaces. Through examination of the near-field PL spectra extracted from images of individual grains, we further reveal the existence of nanoscale inhomogeneities within the molecular layer which influence both the energy of PL emission and ratio of vibronic sidebands and provide compelling evidence that variations in the degree of resonant coupling are present on length scales comparable to the resolution of the near-field measurement. Together these imaging tools enable a more comprehensive understanding of the molecular-level photophysics of organic semiconductor aggregates to be established, accessed under ambient conditions and not requiring low temperatures or ultra-high vacuum typical of complementary analytical approaches. Such information will be critical for example for the optimisation of individual single photon emitters in quantum communication devices and understanding how defects impact the efficiency and spectral sharpness of LEDs.

1. Introduction

Organic semiconductors, small organic molecules and polymers with sp^2 hybridisation, are interesting platforms to harvest, emit and detect light because they are relatively straightforward and inexpensive to process [1] and their properties can be readily tuned through molecular design [2]. They typically host excitons that are bound to individual molecules or monomers within a polymer chain – so-called Frenkel excitons – which possess large exciton binding energies [3,4] and offsets between singlet and triplet states [5]. Consequently, organic semiconductors are among the state-of-the-art for display and lighting technologies [6] while they also represent materials of interest for quantum and light harvesting applications utilising single-photon emission [7–9] and photon upconversion [10–12].

It is understood that the fundamental processes impacting the photophysics of organic semiconductors arise from contributions from intermolecular excitonic coupling, as described by Kasha [13] and Davydov [14], charge transfer [15,16] and vibrational coupling [8,9,17], which are in turn dramatically influenced by their organisation in supramolecular architectures [18–20]. For example, arrangements in which molecules pack side-by-side (/head-to-tail) give rise to H (/J) aggregates with photoluminescence intensity that is suppressed (/enhanced) and blue (/red) shifted due to positive (/negative) Coulomb coupling between neighbouring molecules. Moreover, the self-assembly of monolayers of organic molecules and polymers on the surface of insulators represents a promising route to address molecular aggregates

This article is part of a special issue entitled: Advances in Chemical Imaging published in Optics Communications.

* Corresponding author. Nanoscale and Microscale Research Centre (nmRC), University of Nottingham, University Park, Nottingham, NG7 2RD, UK.
** Corresponding author.
*** Corresponding author.
E-mail addresses: james.kerfoot3@nottingham.ac.uk (J. Kerfoot), graham.rance@nottingham.ac.uk (G.A. Rance), michael.george@nottingham.ac.uk (M.W. George).

https://doi.org/10.1016/j.optcom.2025.131945
Received 27 February 2025; Received in revised form 23 April 2025; Accepted 29 April 2025
Available online 30 April 2025

with suppressed vibrational coupling and charge transfer, exemplified by experiments showing superradiance from organic molecules adsorbed on alkali halide surfaces [21–24]. More recently, ultra-high vacuum scanning tunnelling microscopy electroluminescence experiments have probed the photophysics of organic molecules on ultra-thin alkali halide films at the single-molecule level [25–27] and have enabled the study of processes such as chemical bond formation and breaking [28,29] and single photon emission [30–32]. Hexagonal boron nitride (hBN) is a particularly promising platform to study molecular self-assembly and the photophysics of individual molecules and aggregates [30,31] due to its atomically flat surface, absence of out-of-plane dangling bonds and insulating nature enabling photoluminescence from surface-bound molecules. Two-dimensional molecular self-assemblies on hBN have been demonstrated to host strong light-matter interactions [33–35] arising from the packing of molecules in addition to chromatic shifts arising from interactions with the substrate [23,36].

Developing analytical tools that enable description and thus feedback for control of the structure and photophysics of supramolecular organic semiconductors is therefore key. Most current approaches towards this end are optical techniques used to extract information such as the orientation of transition dipole moments [18,37,38,66], and address organic molecules on length scales comparable to their intermolecular distances and exciton coherence [31,39]. To unlock the full potential of this class of materials, a multiple length scale analytical approach is required. In this work, we choose monolayers of self-assembled perylene-3,4,9,10-tetracarboxylic-3,4,9,10-diimide molecules (1L-PTCDI), deposited both on the surface of hBN and within few-layer hBN vertical heterostructures, as a model system to test our ability to extract structural information using a combination of polarised-resolved photoluminescence (PL) spectroscopy and near-field optical spectroscopies. Such configurations are attractive as the molecular arrangements of 1L-PTCDI are confined to two dimensions, whilst the formation of vertical heterostructures provide both mechanical and environmental stabilisation for the confined molecular layers. Using polarisation-resolved PL spectroscopy imaging, we examine the distribution of transition dipoles within 1L-PTCDI on hBN extracting the relative orientation of the two molecules within the unit cell and determining the orientation of the molecular aggregates with respect to other aggregates. By combining this information with PL peak energies and the relative intensity of vibronic satellite peaks, we can discriminate between resonant and non-resonant chromatic shifts. We then go on to show that heterostructures of 1L-PTCDI encapsulated in thin hBN layers enable tip-enhanced Raman spectroscopy (TERS) and tip-enhanced photoluminescence (TEPL) to be performed using contact mode atomic force microscopy (AFM) feedback without damaging the molecular layer. This demonstrates that experiments analogous to those conducted under ultra-high vacuum conditions with scanning tunnelling microscopy (STM) feedback can be performed under ambient conditions using a more versatile AFM-based platform (TEPL, TERS and electroluminescence). This approach is immediately applicable to fundamental studies of the optical properties of organic semiconductors and brings us closer to mapping chemical composition and figures-of-merit, such as efficiency and emission linewidth, of device-ready thin films at the single molecule and dimer level.

2. Methods

2.1. PTCDI/hBN preparation

PTCDI/hBN were prepared by micromechanical cleavage of hBN crystallites and transfer to Si + 90 nm SiO_2 substrates using the scotch tape method. hBN loaded 90 nm SiO_2 was then placed in a vacuum chamber (base pressure 1×10^{-8} mbar) and annealed to 450 °C for 60 min before cooling to 150 °C and deposition of between 0.5 and 1.5 ML of PTCDI at a rate of ~0.37 ML/min, monitored by a quartz crystal microbalance.

2.2. hBN/PTCDI/hBN preparation

hBN/PTCDI/hBN vertical heterostructures were prepared using the dry transfer technique presented by Purdie et al. [40] Stamps used to transfer heterostructures were prepared by dropping several millilitres of polycarbonate (PC) in chloroform (5 % by weight) onto a clean glass slide, sandwiching between a second glass slide and sliding apart. The PC films on glass were left to dry for ~1 min before ~10 mm squares were cut using a blade. The 10 mm polycarbonate films were stripped from the glass using scotch tape with a square hole cut out and the freestanding PC membrane supported by scotch tape was then stretched over a 1 × 1 × 1 mm polydimethylsiloxane (PDMS) block on a glass slide. The completed stamps were then mounted on a micromanipulator stage and brought into contact with a hBN flake on Si + 90 nm SiO_2 (prepared by micromechanical cleavage) at 40 °C. The stamp was then retracted to pick up the flake and the process monitored using an optical microscope. The hBN flake on the PC stamp was then aligned to the hBN flake on Si + 90 nm SiO_2 with a 0.5 ML coverage of PTCDI, which was picked up in the same way as the first flake. The hBN/PTCDI/hBN flake was then transferred onto commercially available epitaxial 300 nm Au (111) on mica (Georg-Albert-PVD) by bringing the heterostructure on PC into contact with gold at 150 °C and increasing the temperature to 180 °C before retracting the stamp. Upon retracting the stamp, the hBN/PTCDI/hBN heterostructure was left on gold with the delaminated PC film, that was removed by immersion in chloroform for 30 min.

2.3. Plasmonic probe fabrication

Plasmonic probes for TERS and TEPL were prepared by a three-step process described by Kumar et al. [41] A 300 nm SiO_2 layer was grown by thermal oxidation on commercially available end-of-tip-visibility probes (AppNano Access-FM) using a tube furnace (Carbolite-Gero) set at 1029 °C for 30 min with a 2.66 l/min flow of dry N_2 passed through a H_2O-filled boiling vessel set at 90 °C. The oxidised probes were then placed in an ozone cleaner (Osilla) for 60 min to remove any residual contamination before 100 nm of Ag was deposited by sputtering at a rate of 1.5 Å/s and pressure of ~0.1 mbar in high purity Ar.

2.4. Materials characterisation

Far-field PL measurements were performed using an optical spectrometer (HORIBA LabRAM Evolution) equipped with a frequency doubled 532 nm Nd:YAG excitation laser (Oxxius) and a 100x objective with a numerical aperture of 0.9 and 150 l/mm grating. The spatial resolution of the system was measured to be approximately 400 nm. Polarisation-resolved measurements were performed by varying the polarisation of the incident beam using a motorised λ/2 plate.

Near-field TERS and TEPL measurements were performed using a HORIBA SmartSPM system in a side access (reflection mode) geometry with the same optical spectrometer and 532 nm laser used for far-field measurements. TERS and TEPL measurements were performed in 'SpecTop' mode, in which the probe was operated in contact mode for near-field measurements and in tapping mode for a far-field only reference and when moving between pixels. Measurements were performed using homemade plasmonic probes with a maximum observed PL contrast factor ($C_{PL} = [S_{NF+FF}/S_{FF}]$-1) of 0.56.

3. Results and discussion

PTCDI films on hBN were prepared as described in the Methods section. As previously described in the literature [4,12,36,42], PTCDI organises into a canted packing arrangement in which molecules lie 'head-to-tail' in rows, with adjacent rows counterrotated by a canting angle, ø, as shown in Fig. 1. To determine the differences in the optical signatures of monolayer (1L-) and bilayer (2L-) PTCDI, a 1.5 ML film was grown on hBN and characterised using tapping mode AFM (Fig. 2a),

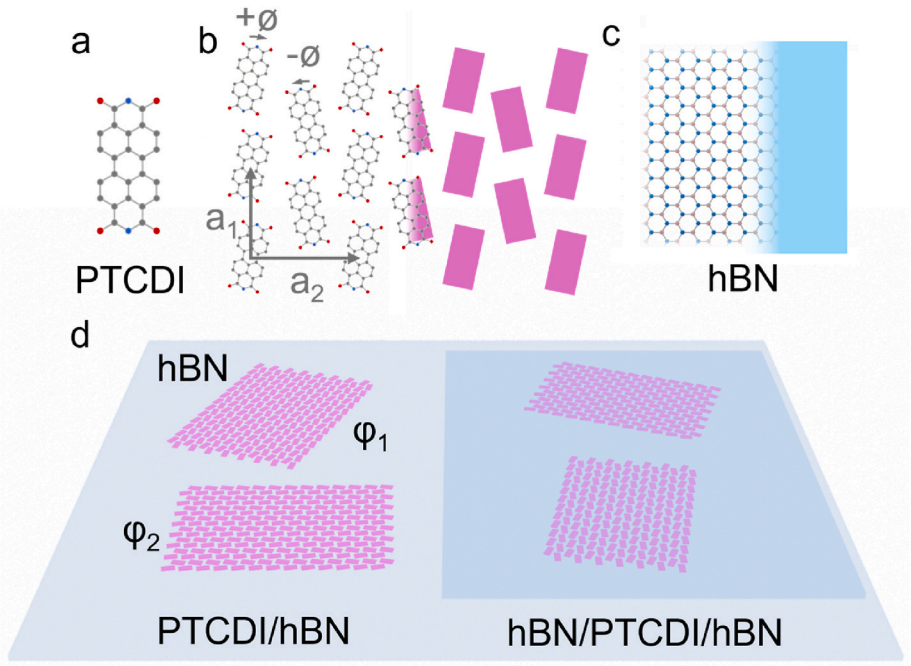

Fig. 1. The molecular structure of PTCDI is shown (a) in addition to its canted packing arrangement (b), in which molecules (simplified as pink rectangles) align in rows where molecules are counterrotated by a canting angle (ø) with respect to the intra-row lattice vector. By depositing molecules onto hBN – the molecular structure of which is shown (simplified as a blue rectangle) (c) – or confining within vertical hBN heterostructures, grains of PTCDI are obtained that may possess differing orientations (φ) with respect to the underlying or overlying hBN flakes (d), with two representative orientations (φ_1 and φ_2) shown. (For interpretation of the references to colour in this figure legend, the reader is referred to the Web version of this article.)

revealing a full coverage of 1L-PTCDI and partial coverage (~29 %) of 2L-PTCDI grains within the 30 × 30 μm scan area. Co-localised PL imaging was then performed which evidenced a decrease in the PL intensity (Fig. 2c) and dramatic red-shift in the emission energy (Fig. 2b and d) over the bilayer regions of the sample relative to the monolayer. The abrupt change in the PL profile between 1L- and 2L-PTCDI arises due to intermolecular charge transfer and vibrational coupling, which are present in multilayer films, but absent in the monolayer where the PTCDI molecules and substrate are co-facial [15,21,33]. Interestingly, in addition to differences between 1L- and 2L-PTCDI, careful inspection of the energy of the peak maximum across both bilayer (Fig. 2d) and monolayer PTCDI (Fig. 2e) revealed two distinct domains in each case, resolvable by their PL emission energies. These are later referred to as type 1 and 2 and possess PL energies of 2.216 ± 0.001 and 2.205 ± 0.001 eV for 1L-PTCDI, respectively. As illustrated in Fig. 2b, the two types of monolayer grain possess very similar linewidths (18.4 ± 0.3 and 16.6 ± 0.4 meV, type 1 and 2, respectively) and 0–1/0-0 peak area ratios (0.147 ± 0.018 and 0.128 ± 0.013, type 1 and 2, respectively). This implies that the observed energy shift does not arise from resonant interactions, which would dramatically alter the PL linewidth and lineshape due to dipole coupling effects [17], rather suggesting a non-resonant origin of the effect related to either molecule-molecule or molecule-substrate interactions. We note that the boundaries of the type 1 and 2 grains and locations of 2L-islands were frequently, but not always, coincident with topographical features, such as step edges and wrinkles of the underlying hBN, as illustrated in Fig. S1 of the Supplementary Information. We interpret such features to likely represent nucleation or termination sites controlling the growth of the 1L- and 2L-islands. Interestingly, the presence of two distinct grain types was not observed for sublimed PTCDI films discussed in our earlier works [42], where the lower spatial resolution in far-field PL measurements and higher areal densities of PTCDI grains on hBN meant multiple grains were addressed simultaneously, which is reflected in our earlier reported 0-0 peak full width at half maximum of 47 meV, significantly higher than the value reported in the present study.

To ascertain the distribution of molecular orientations both within and between grains in the hope of elucidating the origin of the shift in 0-0 PL energy between type 1 and 2 grains of monolayer PTCDI, polarisation-resolved imaging was applied for a sample with only 1L-grains. The dependence of PL response from isolated molecules on laser polarisation is known to follow Malus' law, with maximum emissive intensity observed when the transition dipole moment of the molecule is parallel to the electric field of the excitation source. Therefore, aggregates of organic semiconductors are expected to exhibit a polarisation-resolved PL response that reflects their distribution of transition dipole moment orientations. To perform these measurements, a sample of 0.5 ML coverage of PTCDI containing both grain types and no bilayer regions, was prepared. Subsequent polarisation-resolved PL imaging – whereby a series of hyperspectral images were acquired with incremental increases in incident laser polarisation – revealed the two expected grain types (Fig. 3a). Reassuringly, PL energies of 2.214 ± 0.001 and 2.205 ± 0.002 eV for type 1 and 2, respectively, were observed, commensurate with the analogous grain types noted in monolayer domains of the 1.5 ML sample. As expected, a sinusoidal dependence of the 0-0 PL intensity with a period of 180° was observed for both type 1 and 2 grains (representative data from typical type 1 and 2 grains are shown in Fig. 3b) while the PL line shape was found to be independent of the polarisation (Fig. S2).

To gain further insight, for each pixel of the hyperspectral data set, the polarisation dependence of the 0-0 peak intensity (I(θ)) for the type 1 and 2 grains was measured using a λ/2 plate on a rotational mount. To account for the polarisation response of the instrument grating and spectral filters, a correction factor at each polarisation was applied based upon the intensity of the totally symmetric (polarised) A_1 vibrational mode of carbon tetrachloride. The 1L-PTCDI 0-0 peak intensity at each polarisation was extracted and fitted to a function of the form of Malus' law, $I(\theta) = A\,Cos^2[(\theta - \varphi)] + D$, where θ is the incident laser polarisation, A the difference between minimum and maximum signal and D the signal at minimum intensity. φ corresponds to the angle of strongest PL emission, extracted from fitting, and is used to describe the relative

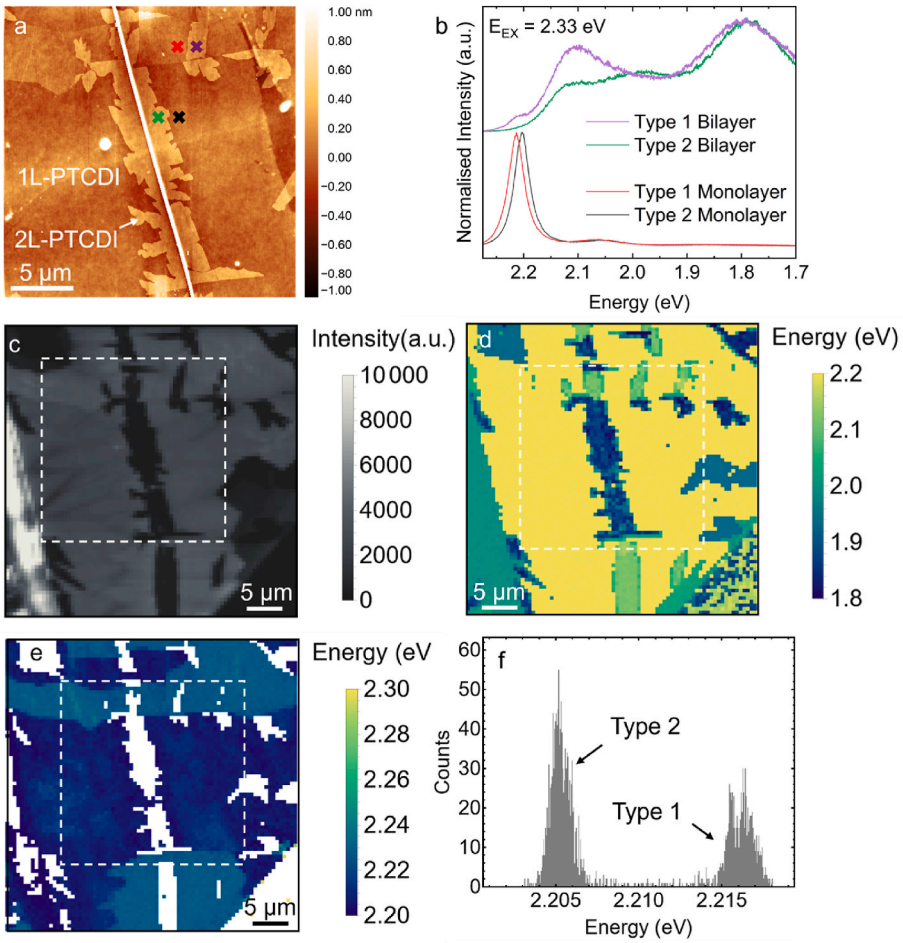

Fig. 2. A 1.5 ML dose of PTCDI deposited at 150 °C on hBN forms a continuous, uniform monolayer with a fractional coverage of second layer grains, as revealed by tapping mode AFM topography imaging (a). Close examination of location-specific PL spectra (b) from the monolayer and bilayer regions (colour coded with respect to their locations as shown in (a)) and the scaled peak position maps, reveal two grain types in both 1L- and 2L-PTCDI with distinct emission energies. Hyperspectral PL imaging (E_{EX} = 2.33 eV) was performed and the extracted 0-0 peak area (c) plotted from the same area as the AFM image in (a), which is represented as a dashed white box in (c), showing a decrease in intensity in the bilayer relative to the monolayer. Differences between the lineshape of type 1 and 2 2L-PTCDI seen in panel (b) were characterised by extracting the position of the pixel of maximum PL intensity between 1.8 and 2.2 eV (d). A spatial map of the 0-0 peak position of 1L-PTCDI was extracted from Lorentzian fitting the same hyperspectral map (e), showing two distinct island types in both the spatial map and a histogram of the fitted 0-0 peak energy from the monolayer (f). (For interpretation of the references to colour in this figure legend, the reader is referred to the Web version of this article.)

orientation of PTCDI islands, as shown in Fig. 1d. Assuming a two-molecule unit cell and an absence of emissive defects within the PTCDI crystal, the polarisation dependence of the PTCDI 0-0 PL intensity follows the form $I(\theta) \alpha (\mathrm{Cos}^2[(\theta + \varphi + \phi)] + \mathrm{Cos}^2[\theta + \varphi - \phi]) = (2\,\mathrm{Cos}^2[\theta + \varphi]\,\mathrm{Cos}[2\phi] + (1 - \mathrm{Cos}[2\phi]))$. Here, ø refers to the canting angle relative to the intra-row lattice vector, as depicted in Fig. 1b, and is determined using the relative intensity of the polarisation dependent PL maxima and minima extracted from fitting [17,38]. The extracted φ and ø parameter maps (Fig. 3c and e, respectively) reveal no significant variation in the relative phase and canting angle within grains, as expected for crystalline two-dimensional aggregates of hydrogen-bonded molecules. By sorting extracted values of φ and ø into type 1 and type 2 datasets based upon 0-0 peak energy thresholding (Fig. 3a) we plot the distribution of extracted φ and ø values for both grain species (Fig. 3d and f, respectively). From this analysis, we determine mean ø values of 15.9 ± 2.6 and 16.9 ± 2.9° for type 1 and 2 grains, respectively, based on fitting the PL polarisation dependence (Fig. 3d). The canting angles estimated from the fitting of type 1 and 2 grains are in good agreement with one another, which suggests that the packing arrangement of the molecules does not differ significantly between grain types. It is important to note that our extracted canting angle values are slightly higher than those obtained from scanning tunnelling microscopy experiments from various substrates (8–13°) [4,12] and prior density functional theory calculations (10.4°) [4]; however, additional depolarisation effects in our measurement arising from both the objective lens (NA: 0.9) and sample likely account for this slight overestimation [43,44]. We also observe several distinct peaks in the histogram of extracted ø values (Fig. 3d) that are clustered at certain φ values (Fig. S2b), though the absence of large spectral shifts and variations in the 0–1/0-0 peak ratio implies that substrate-effects are more significant than resonant and non-resonant shifts arising from molecular packing. These results highlight the utility of extracting the relative orientation of molecules within organic crystals via polarisation-resolved PL [37,38], which is experimentally challenging to do using either AFM under ambient conditions, due to difficulties obtaining the prerequisite spatial resolution to determine molecular orientation, or electron microscopy-based experiments, where the electron beam could potentially damage the sample.

While we are unable to infer the orientation of the underlying hBN substrate, this necessitating techniques such as second harmonic generation or extensive high-resolution AFM characterisation, we can comment on differences in orientation between PTCDI grains. Given the three-fold rotational symmetry of the substrate, we have applied a mod [120°] operator to the extracted φ values and their distribution (Fig. 3f)

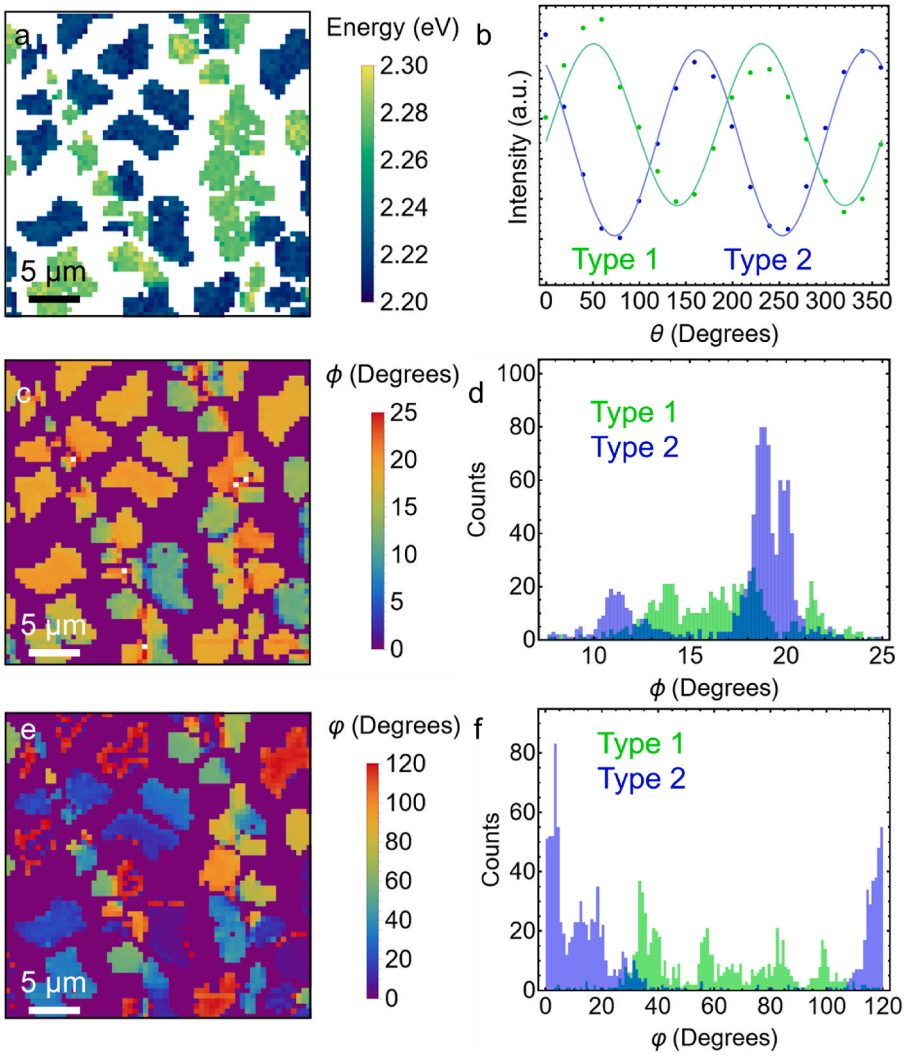

Fig. 3. A second sample of 0.5 ML PTCDI coverage on hBN was prepared (with an areal density of 0.047 μm^{-2}) which evidenced the same type 1 and 2 grains diagnosed by their 0-0 peak energy (a). Polarisation-resolved PL imaging was performed by measuring successive spatial maps and adjusting the linear polarisation of the incident laser using a half-wave plate, with examples of the extracted polarisation dependence of the 0-0 peak intensity from single points for each grain type shown (b). Fitting of the data at each pixel and sorting with respect to grain type enabled extraction of grain-specific ø (c and d) and φ values (e and f), revealing a uniform intra-grain polarisation and clear differences between grain types. Some islands in panel (e) exhibit a high degree of contrast (~0 and ~120°) within islands due to the mod[120°] operator applied to the data. Differentiation between grain types in panels (d) and (f) was done by thresholding the mapped 0-0 peak energy.

which shows several preferred orientations relative to the underlying hBN crystal across both grain types (see further discussion in Fig. S3). A clear difference is seen between the grain species, which sat at distinct orientations with respect to the underlying crystalline hBN. The observation of a distinct grain orientation between type 1 and 2 grains, and absence of notable differences between the 0–1/0-0 peak ratio, peak energy and extracted canting angle of type 1 and 2 grains implies that the spectral shift between grains arises predominantly from the orientation of the molecule relative to the substrate. In our earlier work [36], we used modelling to determine the relative contributions of adsorption to the substrate, intermolecular hydrogen bonding, dielectric environment and dipole-dipole coupling to the spectral shifts relative to isolated molecules. Of the total 399 meV shift from isolated monomers in He droplets [45] to canted 1L-aggregates on hBN, surface adsorption was estimated from density functional theory calculations to contribute 100 meV [36], which is much less than the ~11 meV spectral shift between type 1 and 2 grains seen here. This further supports the assignation of molecule-substrate registry as the origin of the shift as one would expect the interaction between the molecule and substrate to be highly dependent upon registry given the large degree of polarisation within the underlying hBN at the single bond level.

To further exemplify the effect of dielectric environment on the character of molecular PL, an additional sample was prepared comprising a 0.5 ML coverage of PTCDI, i.e., only 1L-grains, confined within two few-layer hBN flakes as described in Methods (in this case the top hBN flake was 1.2 nm thick and the bottom 0.7 nm thick, as confirmed by AFM images shown in Fig. S4). The hBN/PTCDI/hBN heterostructure (Fig. 4a) was transferred to a gold substrate, chosen to enable so-called gap mode TERS and TEPL measurements [46,47], as will be discussed later. An optical micrograph of the completed heterostructure is shown in Fig. 4b, with the morphology of several 1L-PTCDI grains on the few-layer region of the underlying hBN flake outlined in purple. Additional images of the component flakes of the heterostructure acquired during fabrication are also shown in Fig. S4. Hyperspectral PL imaging of the hBN/PTCDI/hBN heterostructure revealed the expected grain morphology (Fig. 4c), with the uniformity of the PTCDI PL emission, its sinusoidal dependence upon polarisation (Fig. S5) and preservation of the observed 0–1/0-0 peak ratio (Fig. 4e) indicating that the far-field PL signal remains dominated by emission from intact aggregates of PTCDI, analogous to the behaviour seen for PTCDI/hBN (Fig. 3).

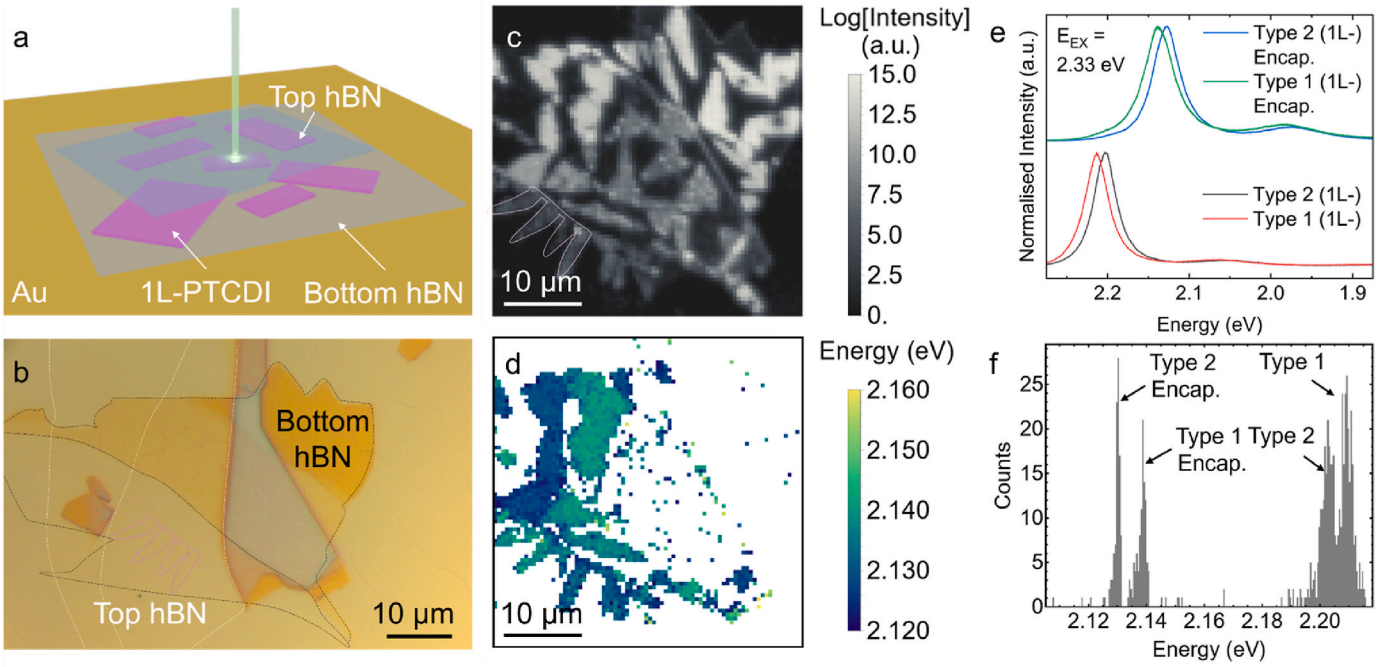

Fig. 4. 1L-PTCDI grains encapsulated within two hBN flakes and transferred onto a gold on mica substrate were prepared (a). Optical microscopy (b) show the structure of the vertical heterostructure, where the edges of the 0.7 nm thick bottom hBN, monolayer PTCDI and 1.2 nm thick top hBN are marked by black, purple and white lines, respectively. Hyperspectral PL imaging of hBN/PTCDI/hBN was performed and the 0-0 peak intensity (c) and energy (d) extracted. Encapsulation in hBN led to a significant red shift in the 0-0 PL energy, with representative PL spectra for type 1 and type 2 grains with and without encapsulation shown (e) in addition to a histogram of the fitted peak energy (f) from panel (d). (For interpretation of the references to colour in this figure legend, the reader is referred to the Web version of this article.)

Interestingly, analysis of the extracted 0-0 PL peak energy (Fig. 4d and e) show that type 1 and 2 grains are present within the vertical heterostructure, though red-shifted by ~76 meV relative to those on a single surface of hBN. The origin of the observed red-shift has been discussed in our earlier work [35] and arises from non-resonant and electrostatic interactions with the substrate. The shift upon encapsulation was found to be 78 ± 1 and 75 ± 2 meV for type 1 and 2 grains, respectively, with a ~35 % increase in the FWHM of the 0-0 peak relative to unencapsulated 1L-PTCDI (21.9 ± 8.2 and 24.8 ± 12 meV for type 1 and 2, respectively). The observation of the shift in the PL upon encapsulation is evidence that a predominantly clean interface is formed between the majority of the emissive 1L-PTCDI and top hBN layer, as the shift would be suppressed by the presence of significant organic contamination. This, combined with our earlier discussion of the 0–1/0-0 peak ratio, polarisation dependence and grain morphology in PL mapping, demonstrates that self-assembled monolayer molecular aggregates may be integrated into layered materials heterostructures [33–35,37]. Interestingly, the only evidence that the 0-0 PL energy may also depend upon the registry of the PTCDI with respect to the second layer was the slight increase in the FWHM of encapsulated versus unencapsulated PTCDI. In this work, we have made no effort to control the relative orientation of the top and bottom hBN lattices, so the two flakes are assumed to be randomly oriented, which would therefore lead to additional structural disorder as the molecules would have different registries with respect to the top and bottom hBN surfaces. Were the registry of the top and bottom hBN flake controlled (a non-trivial task beyond the scope of this work), additional grain types and associated PL emissions may be expected, giving rise to twistronic and moiré [48–50] effects in an organic semiconductor.

To this point, we have presented far-field PL spectroscopy results, which are limited in their spatial resolution by diffraction. Near-field techniques, including TERS and TEPL, enable the chemical composition and photophysics to be studied with in principle near single-molecule spatial resolution and sensitivity and form the basis for the following discussion. TERS and TEPL measurements were performed as discussed in Methods and illustrated in Fig. 5a. The hBN/PTCDI/hBN heterostructure described in Fig. 4 was first characterised using AFM to identify a 1L-PTCDI grain (Fig. 5b), which was found to be type 2 based on its PL signature. AFM topography measurements revealed 1L-PTCDI grains with morphology matching that expected from optical microscopy and PL mapping and with a step height of 0.5 ± 0.4 nm. However, in addition to PTCDI grains, blisters of trapped interfacial contamination not visible using optical microscopy or far-field PL measurements were observed in AFM, which we anticipate were due to atmospheric contaminants present during the sample fabrication, performed under ambient conditions. The AFM measurement shown in Fig. S4 reveals a distinct change in the morphology of blisters between a single hBN flake on gold and a hBN homostructure on gold, in favour of larger and less areally dense blisters within the heterostructure. While smaller field-of-view AFM measurements were unable to discriminate blisters between the bottom hBN layers and Au from those between the PTCDI and the top hBN layers, we infer from this comparative analysis that blisters between hBN and the underlying gold are smaller and less abundant than those between PTCDI and the top hBN (Fig. 5c), which is reflected in the absence of measurable blue-shifted signal in either near- or far-field measurements, which would otherwise indicate non-encapsulated 1L-PTCDI.

TERS and TEPL measurements of the type 2 1L-PTCDI grain were performed with a 532 nm laser and 150 l/mm grating, which provided sufficient spectral range that both TERS and TEPL spectra could be simultaneously acquired. The recorded TERS and TEPL spectra revealed significant differences in the near-field signal with respect to the interfacial blisters. S_{NF} in areas between blisters of trapped contamination were dominated by near-field Raman signal from the PTCDI, with peaks at 1291, 1367 and 1561 cm^{-1} observed, consistent with prior far-field measurements, and tentatively ascribed to the δ(CH)+δ(CC), ν(CN)+δ(CH) and ν(CC)+δ(CH) modes, respectively [45,51,52]. Interestingly, TERS spectra acquired away from encapsulated 1L-PTCDI did not show the peak at ~1366 cm^{-1} (Fig. S6), implying that the resonantly

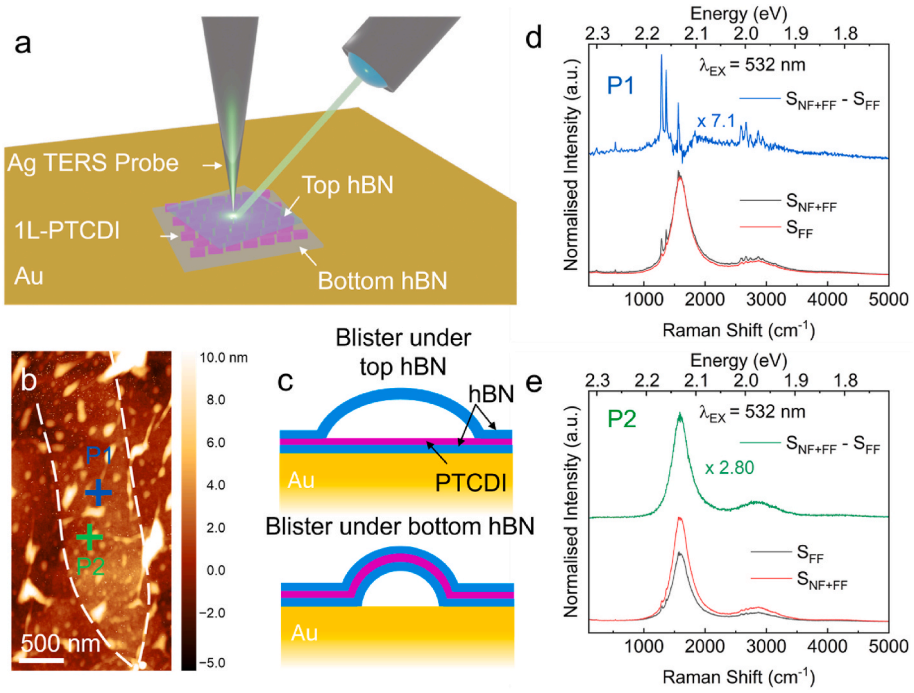

Fig. 5. The formation of thin (few-nanometre thick) hBN/PTCDI/hBN heterostructures on gold enables gap mode TERS and TEPL measurements, as illustrated in (a). Grains of 1L-PTCDI were identified based upon AFM imaging (b) showing both encapsulated grains and blisters of trapped contamination at the Au/hBN, hBN/hBN and PTCDI/hBN interfaces, visible as areas of higher topography. A schematic of blisters between the Au/hBN and PTCDI/hBN interfaces are shown (c), with blisters at the Au/hBN interface believed to be more prevalent based upon comparative AFM imaging (Fig. S2). TERS and TEPL spectra containing contributions from combined near- and far-field (S_{NF+FF}, "tip in"), far-field only (S_{FF}, "tip out") and near-field only (S_{NF}=S_{NF+FF} - S_{FF}) were recorded from areas away from a blister (d), where only the TERS signature of PTCDI was observed, and at the edge of a blister (e), where PTCDI TEPL signal was dominant. The locations of spectra presented in panels (d) and (e) are indicated in panel (b) with blue and green crosses, respectively. The grain was shown to be type 2 based upon the position of the PL peak. (For interpretation of the references to colour in this figure legend, the reader is referred to the Web version of this article.)

enhanced PTCDI TERS signal is stronger than the ν(BN) mode of the substrate [53], though we note the peak at 1367 cm^{-1} could be a convolution of signals from both PTCDI and hBN and therefore expected to be greater in the vertical heterostructure. In areas corresponding to the edges of blisters within the hBN/PTCDI/hBN heterostructure, however, S_{NF+FF} was dominated by near-field PL from the PTCDI to such an extent that near-field Raman peaks were no longer apparent. As the position and line shape of the type 2 1L-PTCDI TEPL peak at 2.132 ± 0.001 eV suggests that the material was fully encapsulated within hBN, we attribute the disparity in the relative intensity of near-field Raman and PL signals to arise from differences in either the junction distance between the gold substrate and PTCDI or the angle at which the molecules are inclined relative to the probe, modulated by blisters in the heterostructure, which would in turn lead to differences in the degree of plasmonic enhancement and quenching [31,54,55]. As the Raman scattering mechanism is more sensitive to the magnitude of the electric field at the probe apex and less sensitive to exciton decay pathways than PL, the greater degree of separation between the 1L-PTCDI and Au that occurs due to contamination trapped at the hBN/Au interface would be expected to favour PL emission. It is also conceivable that the alignment of Raman displacements and PL transition dipole moments versus the effective dipole of the plasmonic probe, as discussed in the literature [56–58], could contribute to differences at blister edges. Moreover, it may be the case that hBN encapsulation may lead to an increase in Raman intensity due to environmental pressure, as reported by Vasu et al. [59] Regardless of the origin of the observed effect, our experimental measurements clearly show that hBN encapsulation provides the ideal platform to study organic molecules using TERS with using AFM feedback; whereas most state-of-the-art TERS and TEPL experiments are performed under ultra-high vacuum conditions with scanning tunnelling microscopy [60–62], by encapsulating molecular systems in hBN sandwich architectures we can explore their physicochemical properties under ambient conditions, with enriched experimental flexibility and potential to tune the magnitude of near-field signals as a function of the substrate-molecule junction.

Returning to the observed TEPL from the edges of blisters in hBN/PTCDI/hBN heterostructures, TEPL imaging was undertaken which showed that the most intense PL emission (Fig. 6b) was coincident with areas of higher topography in the accompanying AFM image (Fig. 6a). The pixel size here was 23 nm, close to the tip resolution estimated based upon TERS maps of a carbon nanotube and scanning electron micrographs of the Ag tip (Fig. S7). Comparing the extracted TEPL spectra from different areas revealed an interesting behaviour, namely a spatial variation in both the 0-0 peak position and the ratio of the 0–1/0-0 peak ratio, which can be clearly seen for three selected spectra plotted (Fig. 6c). Changes in the 0-0/0-1 peak ratio likely arise from changes in resonant coupling between adjacent molecules, namely changes in the degree of J-aggregation [17], while changes in the 0-0 peak energy may arise both as a consequence of J-aggregation, non-resonant effects and changes in dielectric environment [36,63]. To explore the origin of the variation between spectra, each spectrum in the TEPL image shown in Fig. 6b was fit to two Lorentzian peaks in order to extract the 0-0 peak energy and 0–1/0-0 peak ratio. A scatter plot of these values was then plotted for all pixels where TEPL enhancement was observed (Fig. 6d). This analysis reveals a weak correlation between increasing 0–1/0-0 peak intensity and a blue shift of the 0-0 peak, which suggests that inhomogeneities in resonant coupling [64] are present on length scales comparable to the resolution of the experiment, likely arising from disorder or defects within the molecular layer. This result demonstrates the unique opportunity afforded by TEPL to study organic semiconducting molecules, since resonant effects that could not be addressed in real space using far-field techniques can be probed on length scales comparable to exciton coherence and the molecules themselves [64,65].

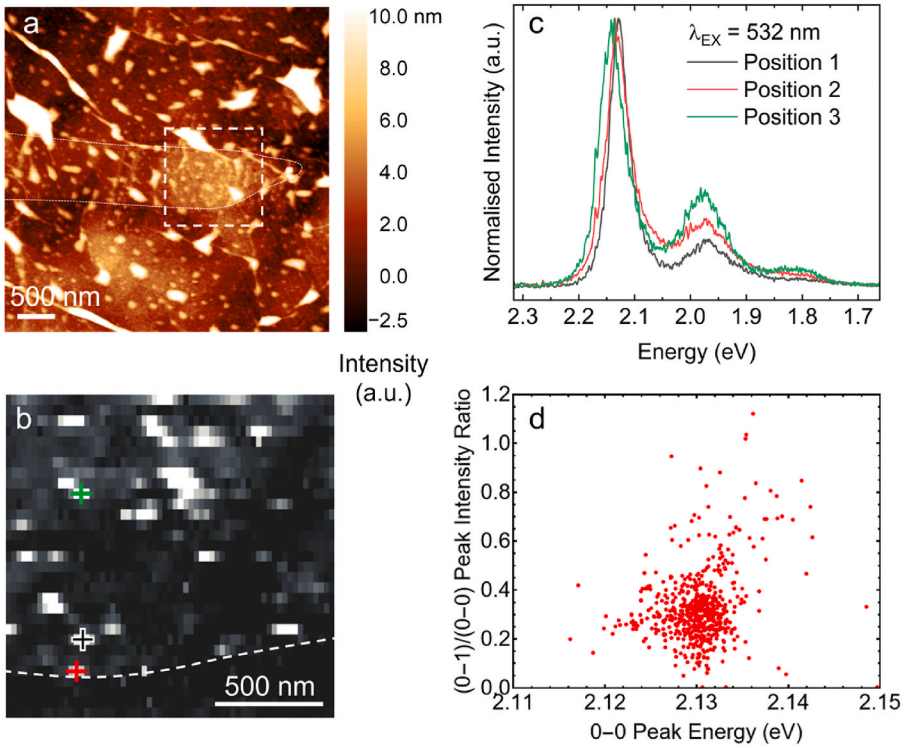

Fig. 6. A TEPL map was acquired from a type 2 island within the region of the hBN/PTCDI/hBN heterostructure on Au marked over a reference AFM image (a). At each pixel of the TEPL map, the near-field only signal was extracted by subtracting a "tip-out" spectrum (S_{NF+FF} - S_{FF}) and fitting the resulting signature with two Lorentzian curves. The intensity of the fitted 0-0 peak was plotted (b) showing areas of higher TEPL emission broadly colocalised with the edges of blisters seen in AFM topography (a). An analogous effect was seen in type 1 islands also (Figs. S8 and S9). Representative TEPL spectra from different areas of brighter emission are marked in panel (b) and plotted (c). The ratio of the fitted 0-0 and 0–1 peaks extracted from fitting is shown plotted against the 0-0 peak energy (d).

4. Conclusions

Using a combination of polarisation-resolved and near-field PL imaging, we explore how molecular packing, substrate registry and local dielectric environment impact the optical properties of self-assembled molecular layers. We show that spatial mapping of 1L-PTCDI on hBN enabled the identification of two separate grain types with distinct substrate registries, confirmed through polarisation-dependent measurements, which were used to extract the intra- and inter-grain orientation of molecules. The formation of heterostructures of 1L-PTCDI encapsulated within few-layer hBN facilitated TERS and TEPL measurements with AFM feedback that (i) preserved the integrity of the molecular layer and (ii) enabled both chemical identification of the molecular species via TERS as well as insights into spatial inhomogeneity of resonant interactions via TEPL. Our results demonstrate the range of information that can be extracted through the application of four-dimensional polarisation-resolved far-field PL mapping and near-field spectroscopy imaging, thus enabling assessment of the impact of molecular aggregate structure on their photophysics expressed at the micro and nano length scales. Furthermore, our work offers new opportunities to unite approaches that study organic films at the device level with ultra-high vacuum-based techniques that explore such materials at the molecular level to assist the development of organic optoelectronic devices with performance commensurate with the intrinsic properties of their constituent molecules.

CRediT authorship contribution statement

James Kerfoot: Writing – review & editing, Writing – original draft, Investigation, Formal analysis, Conceptualization. **Tyler James:** Investigation, Formal analysis. **Takashi Taniguchi:** Resources. **Kenji Watanabe:** Resources. **Peter H. Beton:** Formal analysis. **Graham A. Rance:** Writing – review & editing, Writing – original draft, Supervision, Funding acquisition, Formal analysis. **Michael W. George:** Writing – review & editing, Writing – original draft, Supervision, Funding acquisition.

Disclosures

The authors declare no competing financial interests.

Declaration of competing interest

The authors declare that they have no known competing financial interests or personal relationships that could have appeared to influence the work reported in this paper.

Acknowledgements

J.K, G.A.R and M.W.G acknowledge funding from the Engineering and Physical Science Research Council (EPSRC) (Project: EP/V053884/1), and technical support from the Nanoscale and Microscale Research Centre (nmRC) and the School of Physics and Astronomy, specifically Martin Roe (nmRC) and Jasbinder Chauhan (School of Physics and Astronomy) for assisting with configuration of instrumentation for the plasmonic probe fabrication. K.W. and T.T. acknowledge support from the JSPS KAKENHI (Grant Numbers 21H05233 and 23H02052), the CREST (JPMJCR24A5), JST and World Premier International Research Center Initiative (WPI), MEXT, Japan.

Appendix. ASupplementary data

Supplementary data to this article can be found online at https://doi.org/10.1016/j.optcom.2025.131945.

Data availability

Data will be made available on request.

References

[1] L. Ding, Z.-D. Yu, X.-Y. Wang, Z.-F. Yao, Y. Lu, C.-Y. Yang, J.-Y. Wang, J. Pei, Polymer semiconductors: synthesis, processing, and applications, Chem. Rev. 123 (12) (2023) 7421–7497, https://doi.org/10.1021/acs.chemrev.2c00696.

[2] H. Bronstein, C.B. Nielsen, B.C. Schroeder, I. McCulloch, The role of chemical design in the performance of organic semiconductors, Nat. Rev. Chem 4 (2) (2020) 66–77, https://doi.org/10.1038/s41570-019-0152-9.

[3] A. Sugie, K. Nakano, K. Tajima, I. Osaka, H. Yoshida, Dependence of exciton binding energy on bandgap of organic semiconductors, J. Phys. Chem. Lett. 14 (50) (2023) 11412–11420, https://doi.org/10.1021/acs.jpclett.3c02863.

[4] M. Mura, F. Silly, G.A.D. Briggs, M.R. Castell, L.N. Kantorovich, H-bonding supramolecular assemblies of PTCDI molecules on the Au(111) surface, J. Phys. Chem. C 113 (52) (2009) 21840–21848, https://doi.org/10.1021/jp908046t.

[5] A. Köhler, H. Bässler, Triplet states in organic semiconductors, Mater. Sci. Eng. R Rep. 66 (4) (2009) 71–109, https://doi.org/10.1016/j.mser.2009.09.001.

[6] G. Hong, X. Gan, C. Leonhardt, Z. Zhang, J. Seibert, J.M. Busch, S. Bräse, A brief history of OLEDs—emitter development and industry milestones, Adv. Mater. 33 (9) (2021) 2005630, https://doi.org/10.1002/adma.202005630.

[7] C. Toninelli, I. Gerhardt, A.S. Clark, A. Reserbat-Plantey, S. Götzinger, Z. Ristanović, M. Colautti, P. Lombardi, K.D. Major, I. Deperasińska, et al., Single organic molecules for photonic quantum technologies, Nat. Mater. 20 (12) (2021) 1615–1628, https://doi.org/10.1038/s41563-021-00987-4.

[8] G.D. Scholes, A molecular perspective on quantum information, Proc. R. Soc. A Math. Phys. Eng. Sci. 479 (2279) (2023) 20230599, https://doi.org/10.1098/rspa.2023.0599.

[9] Y. Zhang, C.P. Oberg, Y. Hu, H. Xu, M. Yan, G.D. Scholes, M. Wang, Molecular and supramolecular materials: from light-harvesting to quantum information science and technology, J. Phys. Chem. Lett. 15 (12) (2024) 3294–3316, https://doi.org/10.1021/acs.jpclett.4c00264.

[10] P. Bharmoria, H. Bildirir, K. Moth-Poulsen, Triplet–triplet annihilation based near infrared to visible molecular photon upconversion, Chem. Soc. Rev. 49 (18) (2020) 6529–6554, https://doi.org/10.1039/D0CS00257G.

[11] J. Duan, Y. Liu, Y. Zhang, Z. Chen, X. Xu, L. Ye, Z. Wang, Y. Yang, D. Zhang, H. Zhu, Efficient solid-state infrared-to-visible photon upconversion on atomically thin monolayer semiconductors, Sci. Adv. 8 (2022) 43, https://doi.org/10.1126/sciadv.abq4935, eabq4935.

[12] C. Ludwig, B. Gompf, J. Petersen, R. Strohmaier, W. Eisenmenger, STM investigations of PTCDA and PTCDI on graphite and MoS_2. A systematic study of epitaxy and STM image contrast, Z. Phys. B Condens. Matter 93 (3) (1994) 365–373, https://doi.org/10.1007/BF01312708.

[13] M. Kasha, H.R. Rawls, M. Ashraf El-Bayoumi, The exciton model in molecular spectroscopy 11 (3–4) (1965) 371–392, https://doi.org/10.1351/pac196511030371.

[14] A.S. Davydov, The theory of molecular excitons, Sov. Phys. Usp. 7 (2) (1964) 145, https://doi.org/10.1070/PU1964v007n02ABEH003659.

[15] M. Hoffmann, K. Schmidt, T. Fritz, T. Hasche, V.M. Agranovich, K. Leo, The lowest energy Frenkel and charge-transfer excitons in quasi-one-dimensional structures: application to MePTCDI and PTCDA crystals, Chem. Phys. 258 (1) (2000) 73–96, https://doi.org/10.1016/S0301-0104(00)00157-9.

[16] N.J. Hestand, F.C. Spano, Molecular aggregate photophysics beyond the Kasha model: novel design principles for organic materials, Acc. Chem. Res. 50 (2) (2017) 341–350, https://doi.org/10.1021/acs.accounts.6b00576.

[17] N.J. Hestand, F.C. Spano, Expanded theory of H- and J-molecular aggregates: the effects of vibronic coupling and intermolecular charge transfer, Chem. Rev. 118 (15) (2018) 7069–7163, https://doi.org/10.1021/acs.chemrev.7b00581.

[18] T. Eder, T. Stangl, M. Gmelch, K. Remmerssen, D. Laux, S. Höger, J.M. Lupton, J. Vogelsang, Switching between H- and J-type electronic coupling in single conjugated polymer aggregates, Nat. Commun. 8 (1) (2017) 1641, https://doi.org/10.1038/s41467-017-01773-0.

[19] S. Ma, S. Du, G. Pan, S. Dai, B. Xu, W. Tian, Organic molecular aggregates: from aggregation structure to emission property, Aggregate 2 (4) (2021) e96, https://doi.org/10.1002/agt2.96.

[20] F.C. Spano, C.H.- Silva, J-aggregate behavior in polymeric semiconductors, Annu. Rev. Phys. Chem. 65 (2014) 477–500, https://doi.org/10.1146/annurev-physchem-040513-103639.

[21] H. Proehl, T. Dienel, R. Nitsche, T. Fritz, Formation of solid-state excitons in ultrathin crystalline films of PTCDA: from single molecules to molecular stacks, Phys. Rev. Lett. 93 (9) (2004) 097403, https://doi.org/10.1103/PhysRevLett.93.097403.

[22] T. Dienel, C. Loppacher, S.C.B. Mannsfeld, R. Forker, T. Fritz, Growth-mode-Induced narrowing of optical spectra of an organic adlayer, Adv. Mater. 20 (5) (2008) 959–963, https://doi.org/10.1002/adma.200701684.

[23] M. Müller, E. Le Moal, R. Scholz, M. Sokolowski, Exciton and polarization contributions to optical transition energies in an epitaxial organic monolayer on a dielectric substrate, Phys. Rev. B 83 (24) (2011) 241203, https://doi.org/10.1103/PhysRevB.83.241203.

[24] M. Müller, A. Paulheim, A. Eisfeld, M. Sokolowski, Finite size line broadening and superradiance of optical transitions in two dimensional long-range ordered molecular aggregates, J. Chem. Phys. 139 (4) (2013) 044302, https://doi.org/10.1063/1.4813521.

[25] Y. Zhang, Y. Luo, Y. Zhang, Y.-J. Yu, Y.-M. Kuang, L. Zhang, Q.-S. Meng, Y. Luo, J.-L. Yang, Z.-C. Dong, et al., Visualizing coherent intermolecular dipole–dipole coupling in real space, Nature 531 (7596) (2016) 623–627, https://doi.org/10.1038/nature17428.

[26] H. Imada, K. Miwa, M. Imai-Imada, S. Kawahara, K. Kimura, Y. Kim, Real-space investigation of energy transfer in heterogeneous molecular dimers, Nature 538 (7625) (2016) 364–367, https://doi.org/10.1038/nature19765.

[27] B. Doppagne, M.C. Chong, E. Lorchat, S. Berciaud, M. Romeo, H. Bulou, A. Boeglin, F. Scheurer, G. Schull, Vibronic spectroscopy with submolecular resolution from STM-induced electroluminescence, Phys. Rev. Lett. 118 (12) (2017) 127401, https://doi.org/10.1103/PhysRevLett.118.127401.

[28] E. Kazuma, F. Prihatno, J. Jung, M. Trenary, Y. Kim, Single-molecule investigation of plasmonic near-field effects on a dissociation reaction, J. Phys. Chem. Lett. 16 (7) (2025) 1810–1816, https://doi.org/10.1021/acs.jpclett.4c03564.

[29] A. Rosławska, K. Kaiser, M. Romeo, E. Devaux, F. Scheurer, S. Berciaud, T. Neuman, G. Schull, Submolecular-scale control of phototautomerization, Nat. Nanotechnol. 19 (6) (2024) 738–743, https://doi.org/10.1038/s41565-024-01622-4.

[30] C.C. Leon, O. Gunnarsson, D.G. de Oteyza, A. Rosławska, P. Merino, A. Grewal, K. Kuhnke, K. Kern, Single photon emission from a plasmonic light source driven by a local field-induced Coulomb blockade, ACS Nano 14 (4) (2020) 4216–4223, https://doi.org/10.1021/acsnano.9b09299.

[31] L. Zhang, Y.-J. Yu, L.-G. Chen, Y. Luo, B. Yang, F.-F. Kong, G. Chen, Y. Zhang, Q. Zhang, Y. Luo, et al., Electrically driven single-photon emission from an isolated single molecule, Nat. Commun. 8 (1) (2017) 580, https://doi.org/10.1038/s41467-017-00681-7.

[32] K. Kaiser, A. Rosławska, M. Romeo, F. Scheurer, T. Neuman, G. Schull, Electrically driven cascaded photon-emission in a single molecule, arXiv:2402.17536 [cond-mat.mes-hall] (2024). https://doi.org/10.48550/arXiv.2402.17536.

[33] H. Zhao, Y. Zhao, Y. Song, M. Zhou, W. Lv, L. Tao, Y. Feng, B. Song, Y. Ma, J. Zhang, et al., Strong optical response and light emission from a monolayer molecular crystal, Nat. Commun. 10 (1) (2019) 5589, https://doi.org/10.1038/s41467-019-13581-9.

[34] J. Kerfoot, S.A. Svatek, V.V. Korolkov, T. Taniguchi, K. Watanabe, E. Antolin, P. H. Beton, Fluorescence and electroluminescence of J-aggregated polythiophene monolayers on hexagonal boron nitride, ACS Nano 14 (10) (2020) 13886–13893, https://doi.org/10.1021/acsnano.0c06280.

[35] S.A. Svatek, J. Kerfoot, A. Summerfield, A.S. Nizovtsev, V.V. Korolkov, T. Taniguchi, K. Watanabe, E. Antolín, E. Besley, P.H. Beton, Triplet excitation and electroluminescence from a supramolecular monolayer embedded in a boron nitride tunnel barrier, Nano Lett. 20 (1) (2020) 278–283, https://doi.org/10.1021/acs.nanolett.9b03787.

[36] J. Kerfoot, V.V. Korolkov, A.S. Nizovtsev, R. Jones, T. Taniguchi, K. Watanabe, I. Lesanovsky, B. Olmos, N.A. Besley, E. Besley, et al., Substrate-induced shifts and screening in the fluorescence spectra of supramolecular adsorbed organic monolayers, J. Chem. Phys. 149 (5) (2018) 054701, https://doi.org/10.1063/1.5041418.

[37] S. Koo, I. Park, K. Watanabe, T. Taniguchi, J.H. Shim, S. Ryu, Extraordinary photostability and Davydov splitting in BN-sandwiched single-layer tetracene molecular crystals, Nano Lett. 21 (15) (2021) 6600–6608, https://doi.org/10.1021/acs.nanolett.1c02009.

[38] D. Kim, S. Lee, J. Park, J. Lee, H.C. Choi, K. Kim, S. Ryu, In-plane and out-of-plane excitonic coupling in 2D molecular crystals, Nat. Commun. 14 (1) (2023) 2736, https://doi.org/10.1038/s41467-023-38438-0.

[39] T.W. Johnson, Z.J. Lapin, R. Beams, N.C. Lindquist, S.G. Rodrigo, L. Novotny, S.-H. Oh, Highly reproducible near-field optical imaging with sub-20-nm resolution based on template-stripped gold pyramids, ACS Nano 6 (10) (2012) 9168–9174, https://doi.org/10.1021/nn303496g.

[40] D.G. Purdie, N.M. Pugno, T. Taniguchi, K. Watanabe, A.C. Ferrari, A. Lombardo, Cleaning interfaces in layered materials heterostructures, Nat. Commun. 9 (1) (2018) 5387, https://doi.org/10.1038/s41467-018-07558-3.

[41] N. Kumar, B.M. Weckhuysen, A.J. Wain, A.J. Pollard, Nanoscale chemical imaging using tip-enhanced Raman spectroscopy, Nat. Protoc. 14 (4) (2019) 1169–1193, https://doi.org/10.1038/s41596-019-0132-z.

[42] J. Kerfoot, V.V. Korolkov, S.A. Svatek, M. Alkhamisi, T. Taniguchi, K. Watanabe, P. W. Parkinson, P.H. Beton, Two-dimensional diffusion of excitons in a perylene diimide monolayer quenched by a fullerene heterojunction, J. Phys. Chem. C 123 (19) (2019) 12249–12254, https://doi.org/10.1021/acs.jpcc.9b01413.

[43] G. Turrell, Analysis of polarization measurements in Raman microspectroscopy, J. Raman Spectrosc. 15 (2) (1984) 103–108, https://doi.org/10.1002/jrs.1250150207.

[44] M. Tanaka, R.J. Young, Review Polarised Raman spectroscopy for the study of molecular orientation distributions in polymers, J. Mater. Sci. 41 (3) (2006) 963–991, https://doi.org/10.1007/s10853-006-6595-7.

[45] M. Wewer, F. Stienkemeier, Laser-induced fluorescence spectroscopy of N,N′-dimethyl 3,4,9,10-perylene tetracarboxylic diimide monomers and oligomers attached to helium nanodroplets, Phys. Chem. Chem. Phys. 7 (6) (2005) 1171–1175, https://doi.org/10.1039/B418896A.

[46] K. Uetsuki, P. Verma, P. Nordlander, S. Kawata, Tunable plasmon resonances in a metallic nanotip–film system, Nanoscale 4 (19) (2012) 5931–5935, https://doi.org/10.1039/C2NR31542D.

[47] R. Wang, Z. He, A.V. Sokolov, D. Kurouski, Gap-mode tip-enhanced Raman scattering on Au nanoplates of varied thickness, J. Phys. Chem. Lett. 11 (10) (2020) 3815–3820, https://doi.org/10.1021/acs.jpclett.0c01021.

[48] R. Ribeiro-Palau, C. Zhang, K. Watanabe, T. Taniguchi, J. Hone, C.R. Dean, Twistable electronics with dynamically rotatable heterostructures, Science 361 (6403) (2018) 690–693, https://doi.org/10.1126/science.aat6981.
[49] M.R. Rosenberger, H.-J. Chuang, M. Phillips, V.P. Oleshko, K.M. McCreary, S. V. Sivaram, C.S. Hellberg, B.T. Jonker, Twist angle-dependent atomic reconstruction and moiré patterns in transition metal dichalcogenide heterostructures, ACS Nano 14 (4) (2020) 4550–4558, https://doi.org/10.1021/acsnano.0c00088.
[50] A. Weston, Y. Zou, V. Enaldiev, A. Summerfield, N. Clark, V. Zólyomi, A. Graham, C. Yelgel, S. Magorrian, M. Zhou, et al., Atomic reconstruction in twisted bilayers of transition metal dichalcogenides, Nat. Nanotechnol. 15 (7) (2020) 592–597, https://doi.org/10.1038/s41565-020-0682-9.
[51] V. Chiș, G. Mile, R. Știufiuc, N. Leopold, M. Oltean, Vibrational and electronic structure of PTCDI and melamine–PTCDI complexes, J. Mol. Struct. 924–926 (2009) 47–53, https://doi.org/10.1016/j.molstruc.2008.12.038.
[52] R. Scholz, M. Schreiber, Linear optical properties of perylene-based chromophores, Chem. Phys. 325 (1) (2006) 9–21, https://doi.org/10.1016/j.chemphys.2005.11.024.
[53] R.J. Nemanich, S.A. Solin, R.M. Martin, Light scattering study of boron nitride microcrystals, Phys. Rev. B 23 (12) (1981) 6348–6356, https://doi.org/10.1103/PhysRevB.23.6348.
[54] R.J. Peña Román, Y. Auad, L. Grasso, F. Alvarez, I.D. Barcelos, L.F. Zagonel, Tunneling-current-induced local excitonic luminescence in p-doped WSe_2 monolayers, Nanoscale 12 (25) (2020) 13460–13470, https://doi.org/10.1039/D0NR03400B.
[55] K. Kuhnke, C. Große, P. Merino, K. Kern, Atomic-scale imaging and spectroscopy of electroluminescence at molecular interfaces, Chem. Rev. 117 (7) (2017) 5174–5222, https://doi.org/10.1021/acs.chemrev.6b00645.
[56] R. Ossikovski, Q. Nguyen, G. Picardi, Simple model for the polarization effects in tip-enhanced Raman spectroscopy, Phys. Rev. B 75 (4) (2007) 045412, https://doi.org/10.1103/PhysRevB.75.045412.
[57] Z. Lu, J. Ji, H. Ye, H. Zhang, S. Zhang, H. Xu, Quantifying the ultimate limit of plasmonic near-field enhancement, Nat. Commun. 15 (1) (2024) 8803, https://doi.org/10.1038/s41467-024-53210-8.
[58] H. Miranda, C. Rabelo, L.G. Cançado, T.L. Vasconcelos, B.S. Oliveira, F. Schulz, H. Lange, S. Reich, P. Kusch, A. Jorio, Impact of substrate on tip-enhanced Raman spectroscopy: a comparison between field-distribution simulations and graphene measurements, Phys. Rev. Res. 2 (2) (2020) 023408, https://doi.org/10.1103/PhysRevResearch.2.023408.
[59] K.S. Vasu, E. Prestat, J. Abraham, J. Dix, R.J. Kashtiban, J. Beheshtian, J. Sloan, P. Carbone, M. Neek-Amal, S.J. Haigh, et al., Van der Waals pressure and its effect on trapped interlayer molecules, Nat. Commun. 7 (1) (2016) 12168, https://doi.org/10.1038/ncomms12168.
[60] H. Imada, M. Imai-Imada, K. Miwa, H. Yamane, T. Iwasa, Y. Tanaka, N. Toriumi, K. Kimura, N. Yokoshi, A. Muranaka, et al., Single-molecule laser nanospectroscopy with micro–electron volt energy resolution, Science 373 (6550) (2021) 95–98, https://doi.org/10.1126/science.abg8790.
[61] Y. Luo, S. Sheng, M. Pisarra, A. Martin-Jimenez, F. Martin, K. Kern, M. Garg, Selective excitation of vibrations in a single molecule, Nat. Commun. 15 (1) (2024) 6983, https://doi.org/10.1038/s41467-024-51419-1.
[62] R. Gutzler, M. Garg, C.R. Ast, K. Kuhnke, K. Kern, Light–matter interaction at atomic scales, Nat. Rev. Phys. 3 (6) (2021) 441–453, https://doi.org/10.1038/s42254-021-00306-5.
[63] Y. Lin, X. Ling, L. Yu, S. Huang, A.L. Hsu, Y.-H. Lee, J. Kong, M.S. Dresselhaus, T. Palacios, Dielectric screening of excitons and trions in single-layer MoS_2, Nano Lett. 14 (10) (2014) 5569–5576, https://doi.org/10.1021/nl501988y.
[64] T. Eder, J. Vogelsang, S. Bange, K. Remmerssen, D. Schmitz, S.-S. Jester, T.J. Keller, S. Höger, J.M. Lupton, Interplay between J- and H-type coupling in aggregates of π-conjugated polymers: a single-molecule perspective, Angew. Chem. Int. Ed. 58 (52) (2019) 18898–18902, https://doi.org/10.1002/anie.201912374.
[65] P. Valencia-Acuna, K. Rijal, C.-F. Wang, M. Ziatdinov, W.-L. Chan, P.Z. El-Khoury, Visualizing nanoscale heterogeneity in perylene thin films via tip-enhanced photoluminescence with unsupervised machine learning, Chem. Commun. 60 (58) (2024) 7435–7438, https://doi.org/10.1039/D4CC01808G.
[66] N. le Coutre, T. Abdurakhmonov, P. Weinbrenner, K. Watanabe, T. Taniguchi, T. Korn, F. Fennel, O. Kuhn, F. Reinhard, Growth of few-layer molecular crystals of PTCDI on hexagonal boron nitirde by microspacing air-gap sublimation, ACS Appl. Opt. Mater. 3 (2) (2025) 455–462. https://doi.org/10.1021/acsaom.4c00522.